Temporal-Color Space Analysis of Reflection

Yoichi Sato and Katsushi Ikeuchi

November 30, 1992

CMU-CS-92-207

School of Computer Science
Carnegie Mellon University
Pittsburgh, Pennsylvania 15213-3890

This research was sponsored in part by the Avionics Laboratory, Wright Research and Development Center, Aeronautical Systems Division (AFSC), U. S. Air Force, Wright-Patterson AFB, Ohio 45433-6543 under Contract F33615-90-C-1465 Order No. 7597.

Keywords: Computer vision, color image analysis, photometric stereo, temporal-color space analysis.

Abstract

We proposed a novel method to analyze a sequence of color images. A series of color images are examined in a four dimensional space, which we call *the temporal-color space*, whose axes are the three color axes (RGB) and one temporal axis. The significance of the temporal-color space lies in its ability to represent the change of image color with time. A conventional color space analysis yields the histogram of the colors in an image, only at an instance of time. Conceptually, the two reflection components from the dichromatic reflection model, the specular reflection component and the body reflection component, form two subspaces in the temporal-color space. These two components can be extracted at each pixel in the image locally. Using this fact, we analyzed real color images and separated the two reflection components successfully. We did not make any assumptions about surface properties or the global distribution of surface normals. Finally, object shape was recovered.

This research was sponsored in part by the Avionics Laboratory, Wright Research and Development Center, Aeronautical Systems Division (AFSC), U. S. Air Force, Wright-Patterson AFB, Ohio 45433-6543 under Contract F33615-90-C-1465 Order No. 7597.

Section 1 Introduction

Color spaces, especially the RGB color space, have been widely used by the computer vision community to analyze color images. The first application of color space analysis was image segmentation by partitioning a color histogram into Gaussian clusters [3]. Shafer proposed that, illuminated by a single light source, a cluster of uniformly colored dielectric objects in the color space forms a parallelogram defined by two color vectors, namely the specular reflection vector and the body reflection vector [21]. This is also known as the dichromatic reflectance model [22]. Subsequently, Klinker, Shafer and Kanade [10][11] demonstrated that the cluster actually forms a *T-shape* in the color space instead of a parallelogram, and they separated the body reflection component and the specular reflection component by geometrically clustering a scatter plot of the image in the RGB color space. They used the separated body reflection component for segmentation of a color image without suffering from disturbances of highlights in the image. This method is based on the assumption that the directions of surface normals in an image are widely distributed in all directions. This assumption guarantees that both the body reflection vector and the specular reflection vector will be visible. Therefore, their algorithm cannot handle cases where only a few planar surface patches exist in the image. Recently, Novak and Shafer [18] examined the features of clusters caused by surface roughness and interreflection.

Techniques to separate the two reflection components by using a polarization filter have also been studied. Wolff [26] has shown that the specular reflection component can be successfully separated from the body reflection component in a black and white image by using a polarization filter. Recently, Nayar, Fang and Boult [16] introduced the technique to separate the two reflection components by using polarization in the case of a color image and produced very impressive experimental results.

Two other techniques which have been used to analyze images are *shape from shading* and *photometric stereo*. The shape from shading technique introduced by Horn [7] recovers object shapes from a single intensity image. In this method, surface orientations are calculated starting from a chosen point whose orientation is known *a-priori*, by using the characteristic strip expansion method. Ikeuchi and Horn [8] developed a shape from shading technique which uses occluding boundaries of an object to iteratively calculate surface orientation. Woodham [25] proposed a new technique for shape recovery which uses multiple images with different light source locations. His technique does not rely on assumptions such as the surface smoothness constraint. Nayar, Ikeuchi and Kanade [14] developed a technique for recovering object shape and reflectance without any knowledge of surface reflectance. The techniques used by Woodham and Nayar are collectively called *photometric stereo*; the object shape is recovered based on intensity change due to different light source directions.

In this report, we propose a new technique to analyze object shape and surface properties from color images. We observe how the color of the image changes with a moving light source in a four dimensional "RGB plus light direction" space, which we call the *temporal-color space*. (The temporal-color space is defined in Section 2.3.) The proposed technique does not require any knowledge of surface reflectance. Only *local* information is needed in our analysis. In other words, we can recover the surface orientation and reflectance based on color change at each pixel individually. This method has been successfully applied to real color images, resulting in the decomposition of pixel intensities into the specular and body reflection components, which are subsequently used to recover surface orientation and reflectance.

In Section 2, the temporal-color space is introduced and compared with the spaces currently used in color and photometric analysis. Our proposed algorithm to decompose reflection into the two reflection components in the temporal-color space is described in Section 3. The results of experiments conducted using objects of different types of materials are presented in Section 4. Finally, we conclude this paper in Section 5.

Section 2 Temporal-Color Space

The spaces most commonly used in color space analysis and in photometric stereo are the RGB (Red-Green-Blue) color space and the $I - \theta_s$ (image intensity - light source direction) space, respectively. In this paper, we propose a new space called the "*temporal-color space"* in order to analyze color change with time, which cannot be analyzed in either the RGB color space or the $I - \theta_s$ space. This chapter describes these three spaces and their relationships with one another. Note that in this paper, the term "pixel value" refers to pixel intensity.

2.1. The RGB Color Space

An image intensity I is determined by the spectral distribution of incident light to the camera $h(\lambda)$ and the camera response to the various wavelengths $s(\lambda)$, i.e.,

$$I = \int s(\lambda)\, h(\lambda)\, d\lambda \qquad \textbf{(EQ1)}$$

A color camera has color filters attached in front of its sensor device. Each color filter has a transmittance function $\tau(\lambda)$ which determines the fraction of light transmitted at each wavelength λ. Then, pixel intensities I_R, I_G, and I_B from red, green, and blue channels of the color camera are given by the following integrations:

$$\begin{aligned} I_R &= \int \tau_R(\lambda)\, s(\lambda)\, h(\lambda)\, d\lambda \\ I_G &= \int \tau_G(\lambda)\, s(\lambda)\, h(\lambda)\, d\lambda \\ I_B &= \int \tau_B(\lambda)\, s(\lambda)\, h(\lambda)\, d\lambda \end{aligned} \qquad \textbf{(EQ2)}$$

where $\tau_R(\lambda), \tau_G(\lambda), \tau_B(\lambda)$ are the transmittance functions of the red filter, green, and blue filters, respectively. The three intensities I_R, I_G and I_B form a 3×1 color vector $\vec{C}$ which represents the color of a pixel in the RGB color space.

$$\vec{C} = \begin{bmatrix} I_R \\ I_G \\ I_B \end{bmatrix} = \begin{bmatrix} \int \tau_R(\lambda)\, s(\lambda)\, h(\lambda)\, d\lambda \\ \int \tau_G(\lambda)\, s(\lambda)\, h(\lambda)\, d\lambda \\ \int \tau_B(\lambda)\, s(\lambda)\, h(\lambda)\, d\lambda \end{bmatrix} \qquad \textbf{(EQ3)}$$

Klinker, Shafer, and Kanade [10][11] demonstrated that the histogram of dielectric object color in the RGB color space forms a T-shape (Figure 1). They clustered the two components of the T-shape in order to separate the specular reflection component and the body reflection component.

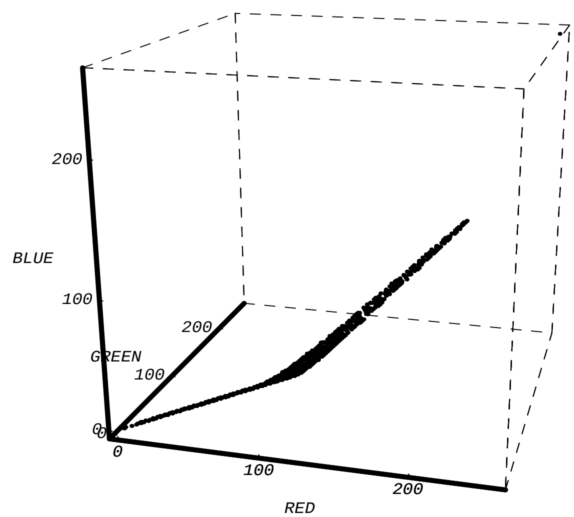

Figure 1 T-shape in the RGB color space (synthesized data)

A significant limitation of the method is that it works only when surface normals in the image are well distributed in all directions. Suppose that the image has only one planar object illuminated by a light source which is located far away from the object. Then, all pixels on the object are mapped to a single point in the color space because observed color is constant over the object surface. The T-shape converges to a single point in the RGB color space which represents the color of the object, because the plane has uniform color. As a result, we cannot separate the reflection components. This indicates the dependence of the method on global information, and thus it cannot be applied locally.

2.2. The $I-\theta_s$ (Intensity - Light source direction) Space

Nayar, Ikeuchi, and Kanade [14] analyzed an image sequence given by a moving light source in the $I-\theta_s$ space. They consider how the pixel intensity changes as the light source direction, θ_s, varies in the *viewer-centered coordinate system* (Figure 2).

The pixel intensity from a monochrome camera is written as a function of θ_s:

$$I(\theta_s) = g(\theta_s) \int s(\lambda)\, h(\lambda)\, d\lambda \quad \textbf{(EQ4)}$$

where $g(\theta_s)$ represents intensity change with respect to a light source direction θ_s. Note that the spectral distribution of incident light to the camera $h(\lambda)$ is generally dependent on geometric relations such as the viewing direction and the illumination direction. However, as an approximation, we assume that the function $h(\lambda)$ is independent of these factors.

The vector $p(\theta_s, I(\theta_s))$ shows how pixel intensity changes with respect to light source direction in $I - \theta_s$ space (Figure 3).

As opposed to analysis in the RGB color space, the $I - \theta_s$ space analysis is applied locally. All necessary information is extracted from the intensity change at each individual pixel. Nayar used the $I - \theta_s$ space to separate the surface reflection component and the body reflection component, using *a-priori* knowledge of the geometry of the “photometric sampler” [14].

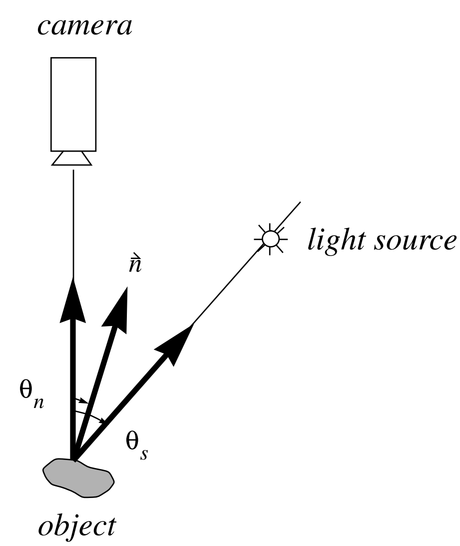

Figure 2 The viewer centered coordinate system

$\vec{n}$ is a surface normal and θ_s and θ_n denote the angle between the viewing direction and the light source direction and the angle between the viewing direction and the surface normal.

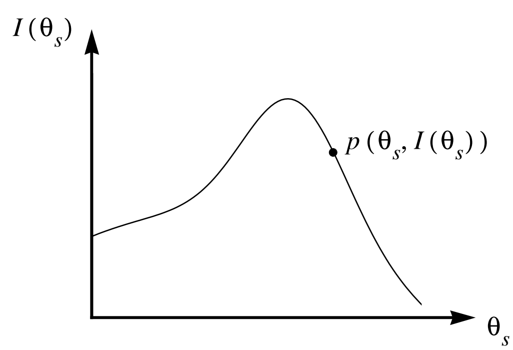

Figure 3 The $I - \theta_s$ space

2.3. The Temporal-Color Space

Neither the RGB color space nor the $I - \theta_s$ space can be used to separate the two reflection components using local pixel information without resorting to relatively strong assumptions. To address this weakness, we propose a new four dimensional space, which we call the *temporal-color space*. The four dimensional space is spanned by the R, G, B, and θ_S axes. The term "temporal-color space" implies an augmentation of the RGB color space with an additional dimension that varies with time. This dimension represents the geometric relationship between the viewing direction, illumination direction, and surface normal. In our paper, we keep the viewing direction and surface normal orientation fixed. We vary the illumination direction with time, taking a new image at each new illumination direction. (The same information could be obtained if we kept the illumination direction and surface normal's orientation fixed, and varied the viewing direction, or if we kept the viewing direction and illumination direction fixed, and varied the surface normal orientation.)

The temporal-color space can be thought of as a union of the RGB color space and the $I - \theta_s$ space. By omitting the θ_s axis, the temporal-color space becomes equivalent to the RGB color space, and by omitting two color axes, the temporal-color space becomes the $I - \theta_s$ space. Each point in the space is represented by the light source direction θ_s and the color vector $\vec{C}(\theta_s)$ which is a function of θ_s:

$$p\left(\theta_s, \vec{C}(\theta_s) \right) \qquad \textbf{(EQ5)}$$

$$\vec{C}(\theta_s) = \begin{bmatrix} I_R(\theta_s) \\ I_G(\theta_s) \\ I_B(\theta_s) \end{bmatrix} = \begin{bmatrix} g(\theta_s) \int \tau_R(\lambda)\, s(\lambda)\, h(\lambda)\, d\lambda \\ g(\theta_s) \int \tau_G(\lambda)\, s(\lambda)\, h(\lambda)\, d\lambda \\ g(\theta_s) \int \tau_B(\lambda)\, s(\lambda)\, h(\lambda)\, d\lambda \end{bmatrix} \qquad \textbf{(EQ6)}$$

The temporal-color space represents how the observed color of a pixel $\vec{C}(\theta_s)$ changes with time while the direction of the light source θ_s changes (Figure 4). Note that, in Figure 4, the dimension of the temporal-color space is reduced from four to three for clarity. In this diagram, one axis of the RGB color space is ignored.

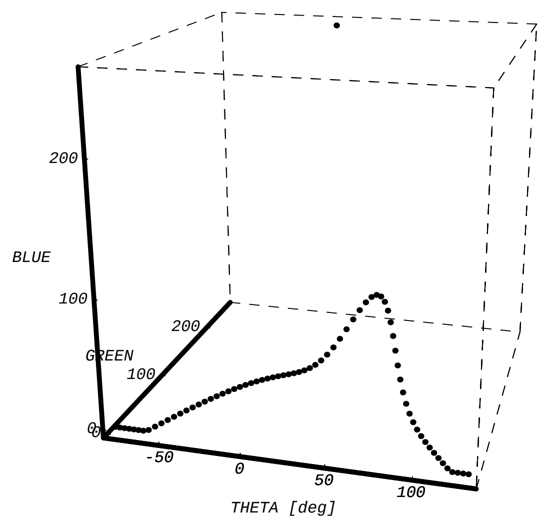

Figure 4 The temporal-color space (synthesized data)

Section 3 Decomposition of Reflection

3.1. Reflectance model

The hybrid reflectance model (Appendix A) proposed by Nayar, Ikeuchi, and Kanade [14] is used as the reflectance model for dielectric materials in our experiments. From (EQ28) and (EQ29) in Appendix A, the pixel value $I(\theta_s)$ in the viewer-centered coordinate system (Figure 2) is given by:

$$\begin{aligned} I(\theta_s) &= I_{body}(\theta_s) + I_{specular}(\theta_s) \\ &= K_L L(\theta_s - \theta_n)\cos(\theta_s - \theta_n) + K_S L(\theta_s - \theta_n)\,\delta(2\theta_n - \theta_s) \end{aligned} \quad \textbf{(EQ7)}$$

$$\begin{aligned} K_L &= \int_\lambda s(\lambda)\,c(\lambda)\,c_L(\lambda)\,d\lambda \\ K_S &= c_s \int_\lambda s(\lambda)\,c(\lambda)\,d\lambda \end{aligned} \quad \textbf{(EQ8)}$$

where $c(\lambda)$ is the spectral distribution of incident light. $L(\theta_s - \theta_n)$ is the geometrical term of the incident light (EQ26). $s(\lambda)$ is the spectral response of the camera. $c_L(\lambda)$ and c_S are the spectral reflectance distributions of the body reflection component and the specular reflection component, respectively (EQ23). In (EQ7) and (EQ8), $L(\theta_s - \theta_n)\cos(\theta_s - \theta_n)$ and $L(\theta_s - \theta_n)\,\delta(2\theta_n - \theta_s)$ correspond to $g(\theta_s)$ in (EQ4). $c(\lambda)\,c_L(\lambda)$ and $c_s c(\lambda)$ correspond to $h(\lambda)$ in (EQ4).

$I(\theta_s)$ for an extended light source obeys the following formula (Appendix B):

$$I(\theta_s) = K_L \cos(\theta_s - \theta_n) + K_S L(\theta_s - 2\theta_n) \quad \textbf{(EQ9)}$$

The hybrid reflectance model is valid when there is no interreflection and there is only one light source. Therefore, our algorithm cannot be applied when there is interreflection, or when there are multiple light sources with different spectral distributions. Our algorithm can only be applied to images taken under the illumination of a single spectral distribution, in the absence of interreflection.

3.2. Decomposition of reflection in the temporal-color space

In this section, the algorithm used to separate the two reflection components in the temporal-color space is described. Using red, green, and blue filters, the coefficients K_L and K_S, in (EQ8), become two linearly independent vectors, $\underset{\sim}{K}_L$ and $\underset{\sim}{K}_S$, unless the colors of the two reflection components are accidentally same:

$$\underset{\sim}{K}_L = \begin{bmatrix} k_{LR} \\ k_{LG} \\ k_{LB} \end{bmatrix} = \begin{bmatrix} \int_\lambda \tau_R(\lambda)\, s(\lambda)\, c(\lambda)\, c_L(\lambda)\, d\lambda \\ \int_\lambda \tau_G(\lambda)\, s(\lambda)\, c(\lambda)\, c_L(\lambda)\, d\lambda \\ \int_\lambda \tau_B(\lambda)\, s(\lambda)\, c(\lambda)\, c_L(\lambda)\, d\lambda \end{bmatrix} \qquad \textbf{(EQ10)}$$

$$\underset{\sim}{K}_S = \begin{bmatrix} k_{SR} \\ k_{SG} \\ k_{SB} \end{bmatrix} = \begin{bmatrix} c_S \int_\lambda \tau_R(\lambda)\, s(\lambda)\, c(\lambda)\, d\lambda \\ c_S \int_\lambda \tau_G(\lambda)\, s(\lambda)\, c(\lambda)\, d\lambda \\ c_S \int_\lambda \tau_B(\lambda)\, s(\lambda)\, c(\lambda)\, d\lambda \end{bmatrix} \qquad \textbf{(EQ11)}$$

These two vectors represent the colors of the body and specular reflection components in the dichromatic reflectance model [22].

First, the pixel intensities in the R, G, and B channels with m different light source directions, are measured at one pixel. It is important to note that all intensities are measured *at the same pixel*. The intensity values are shown in Figure 5.

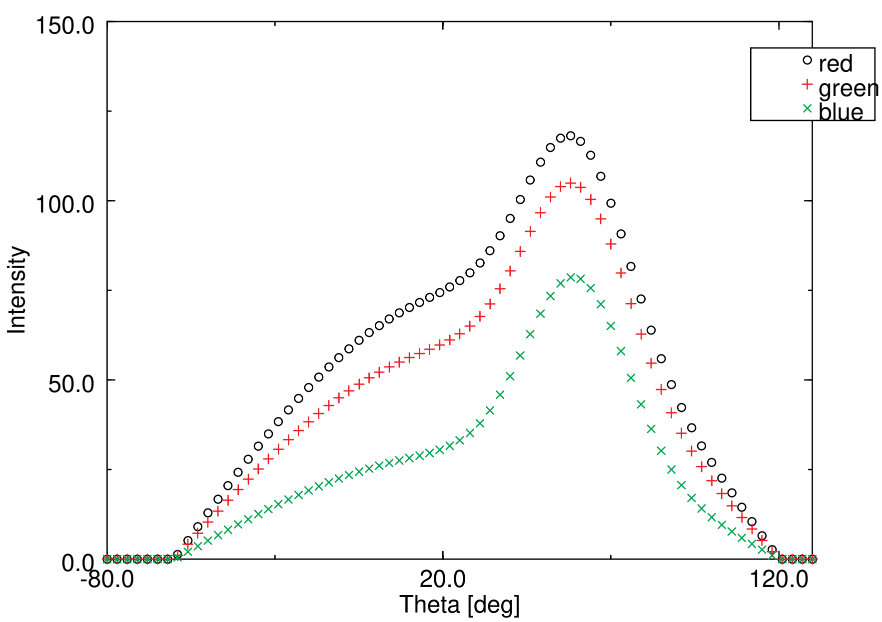

Figure 5 Measurement at one pixel (synthesized data)

The three sequences of intensity values are stored in the columns of an $m \times 3$ matrix I. The matrix is called the *temporal-color matrix*. Considering the hybrid reflectance model and two color vectors in (EQ9), (EQ10), and (EQ11), the intensity values in the R, G, and B channels can be represented as:

$$
\begin{aligned}
I &= \begin{bmatrix} \tilde{I}_R & \tilde{I}_G & \tilde{I}_B \end{bmatrix} \\
&= \begin{bmatrix} \cos(\theta_{s1} - \theta_n) & L(\theta_{s1} - 2\theta_n) \\ \cos(\theta_{s2} - \theta_n) & L(\theta_{s2} - 2\theta_n) \\ \cdot & \cdot \\ \cdot & \cdot \\ \cos(\theta_{sm} - \theta_n) & L(\theta_{sm} - 2\theta_n) \end{bmatrix} \begin{bmatrix} k_{LR} & k_{LG} & k_{LB} \\ k_{SR} & k_{SG} & k_{SB} \end{bmatrix} \\
&= \begin{bmatrix} \tilde{D}_L & \tilde{D}_S \end{bmatrix} \begin{bmatrix} \tilde{K}_L^T \\ \tilde{K}_S^T \end{bmatrix} \\
&\equiv DK
\end{aligned}
\quad \textbf{(EQ12)}
$$

where the two vectors $\tilde{D}_L$ and $\tilde{D}_S$ represent the intensity values of the body and specular reflection components with respect to the light source direction θ_s. Vector $\tilde{K}_L$ represents the body reflection color vector. Vector $\tilde{K}_S$ represents the specular reflection color vector. We call the two matrices D and K, the *geometry matrix* and the *color matrix,* respectively. The color vectors and the θ_s axis span the space in the temporal-color space. We call the space spanned by the color vector $\tilde{K}_L^T$ and the θ_s axis the *body reflection plane*, and the space spanned by the color vector $\tilde{K}_S^T$ and the θ_s axis the *specular reflection plane.*

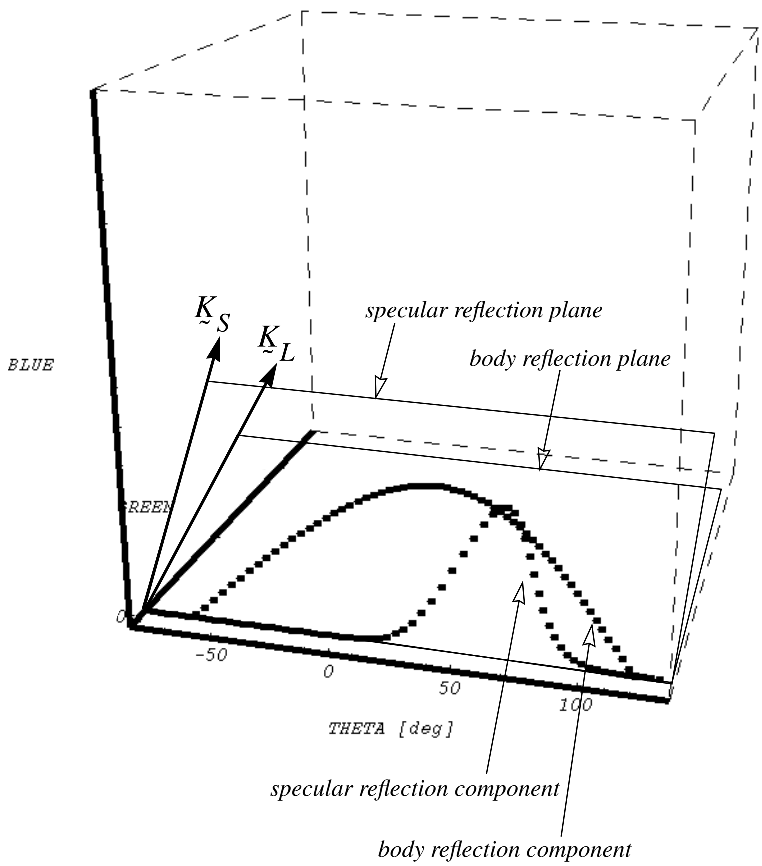

Figure 6 The body reflection place and the specular reflection plane (synthesized data)

In the case of a conductive material, such as metal, (EQ12) becomes

$$I = \begin{bmatrix} \underset{\sim}{I}_R & \underset{\sim}{I}_G & \underset{\sim}{I}_B \end{bmatrix}$$

$$= \begin{bmatrix} L(\theta_{s1} - 2\theta_n) \\ L(\theta_{s2} - 2\theta_n) \\ \cdot \\ \cdot \\ L(\theta_{sm} - 2\theta_n) \end{bmatrix} \begin{bmatrix} k_{SR} & k_{SG} & k_{sB} \end{bmatrix}$$

$$= \underset{\sim}{D}_S \underset{\sim}{K}_S^T \qquad \textbf{(EQ13)}$$

because there exists only the specular reflection component.

Suppose we have an estimation of the color matrix K. Then, the two reflection components represented by the geometry matrix D are obtained by projecting the observed reflection stored in I onto the two color vectors $\underset{\sim}{K}_L$ and $\underset{\sim}{K}_S$.

$$D = IK^{+} \tag{EQ14}$$

where K^{+} is a 3×2 pseudoinverse matrix of the color matrix K.

This derivation is based on the assumption that the color matrix K is known. It can be seen from (EQ11) that the specular reflection color vector is the same as a light source color vector. Several algorithms have been proposed to estimate illuminant color [13][23].

3.2.1. Estimation of the illuminant color

1. According to the dichromatic reflection model [22], the color of reflection from a dielectric object is a linear combination of the body reflection component and the specular reflection component. The color of the specular reflection component is equal to the illuminant color. In the x-y chromaticity diagram, the observed color of the dielectric object lies on a segment whose endpoints represent the colors of the body and specular reflection components. By representing the color of each object as a segment in the chromaticity diagram, the illuminant color can then be determined from the intersection of the two segments attributed to the two objects of interest (Figure 7) [13][23].

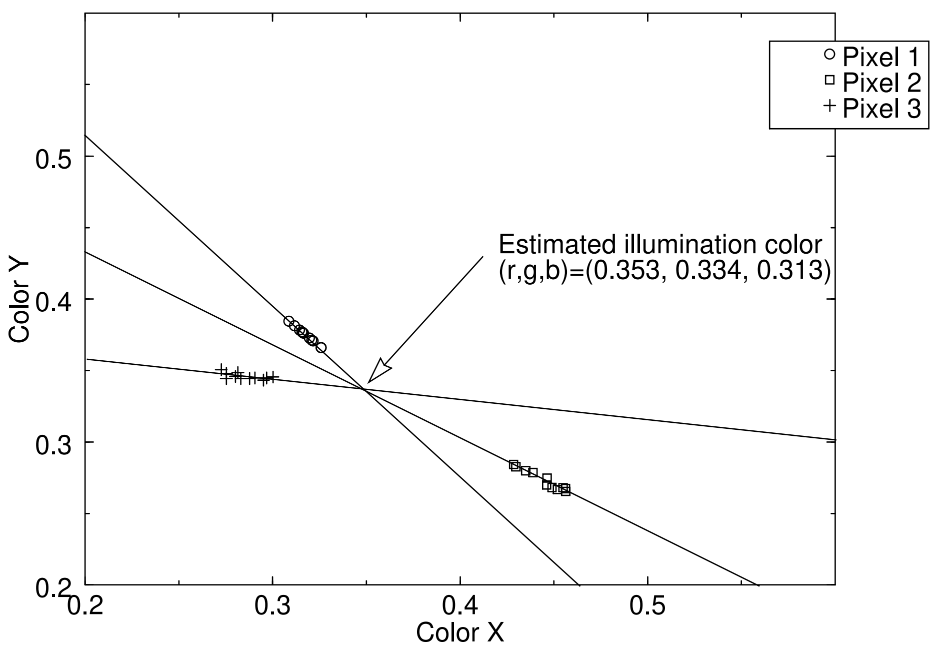

Figure 7 Estimation of illuminant color in the x-y chromaticity diagram
Those three pixels of different colors are manually selected in the image (Figure 27).

2. Tominaga and Wandell [23] indicated that the spectral power distributions of all possible observed color, of a dielectric object with a highlight, exist on the plane spanned by the spectral power distributions of the body reflection component and the specular reflection component. They called this plane the *color signal plane*. Each object color forms its own color plane. The spectral power distribution of the specular reflection component, which is the same as the spectral power distribution of the illuminant, can be obtained by taking the intersection of the color planes. The singular value decomposition technique was used to determine the intersection of color planes.

In our experiment, the row $\underset{\sim}{K}_S^T$ of the color matrix, K, which represents illumination color, is estimated using a method similar to the first method described above.

First, several pixels of different colors in the image are manually selected (Figure 27). The observed reflection color from those selected pixels is a linear combination of the body reflection component and the specular reflection component. By plotting the observed reflection color of each pixel in the x-y chromaticity diagram over the image sequence, we obtain several line segments in the x-y chromaticity diagram. The illuminant color can then be determined by the intersection of those line segments in the diagram. This is shown in Figure 7 for the case of the real image shown in Figure 27.

This technique is limited to the case that there are objects of different colors in the image. In other words, if the image contains objects of only one color, the light source color cannot be estimated. In those cases, the illumination color is obtained by measuring the color vector of the light source directly.

However, the other row $\underset{\sim}{K}_L^T$ of the color matrix cannot be obtained in the same manner because it depends on the material of the object. Fortunately, in order to solve this problem, we can use the fact that the distribution of the specular reflection component for the extended light source is limited to a fixed angle 2α, determined by the geometric relation between the diffuser and the point light source ((EQ30) and (EQ31) in Appendix B). This fact results in the following important lemma.

3.2.2. Estimation of the color vector of the body reflection component

If two vectors, $\underset{\sim}{w}_i = \left[I_{Ri}\ I_{Gi}\ I_{Bi}\right]^T (i = 1, 2)$ are sampled on the θ_s axis at an interval greater than 2α, at least one of these vectors is equal to the color vector of the body reflection component $\underset{\sim}{K}_L^T$. This vector has no specular reflection component. It is guaranteed that both vectors $\underset{\sim}{w}_i$ exist in the row space of the color matrix K spanned by the basis $\underset{\sim}{K}_L^T$ and $\underset{\sim}{K}_S^T$. Therefore, the desired color vector of the body reflection component $\underset{\sim}{K}_L^T$ is the vector $\underset{\sim}{w}_i$ which subtends the largest angle with respect to the vector $\underset{\sim}{K}_S^T$ (Figure

8). The angle between the two color vectors can be calculated as:

$$\beta = \operatorname{acos}\frac{\underset{\sim}{K}_S^T \cdot \underset{\sim}{w}_i}{\left|\underset{\sim}{K}_S^T\right|\left|\underset{\sim}{w}_i\right|} \tag{EQ15}$$

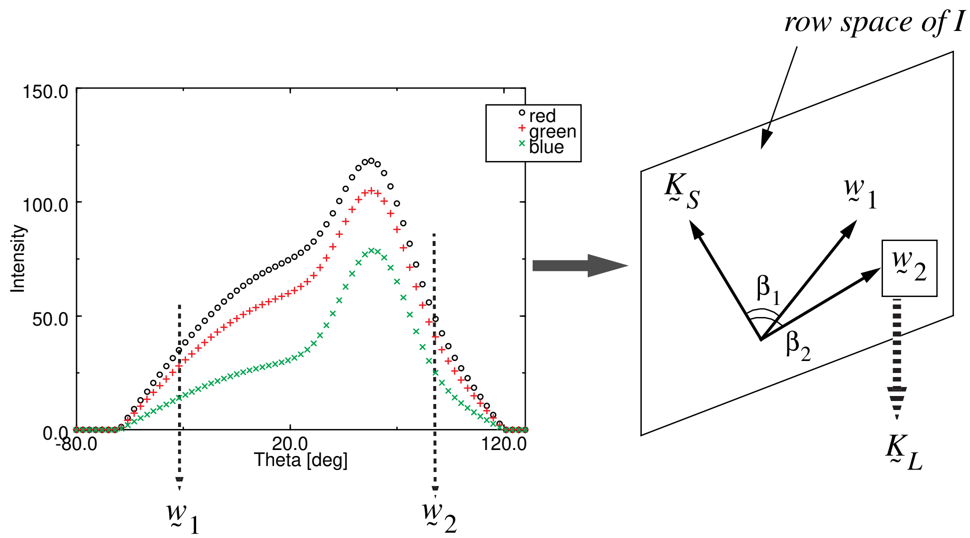

Figure 8 The estimation of the color vector $\underset{\sim}{K}_L^T$

$$D = \begin{bmatrix}\underset{\sim}{D}_L & \underset{\sim}{D}_S\end{bmatrix} = \begin{vmatrix} D_L^1 & D_S^1 \\ D_L^2 & D_S^2 \\ \dots & \dots \\ D_L^m & D_S^m \end{vmatrix}$$

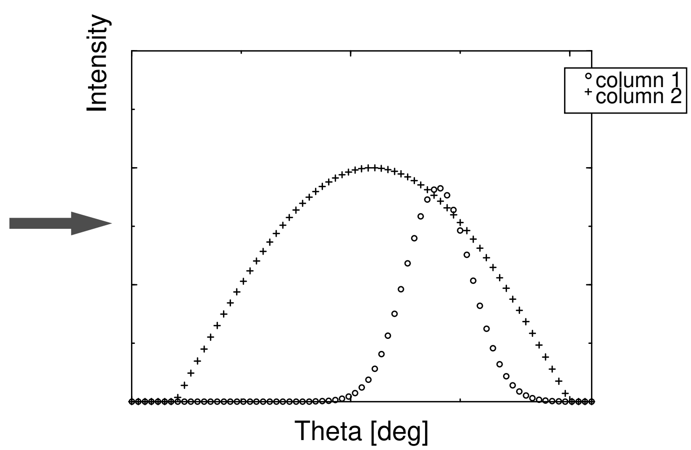

Figure 9 The geometry matrix D (synthesized data)

Once we get the color matrix K, the geometry matrix D can be calculated from (EQ14) (Figure 9).

Once the matrix D has been obtained, the loci of the body reflection component and the specular reflection component in the temporal-color space can be extracted as shown in (EQ16) and (EQ17):

$$I_{body} = \underset{\sim}{D}_L \underset{\sim}{K}_L^T \tag{EQ16}$$

$$I_{specular} = \underset{\sim}{D}_S \underset{\sim}{K}_S^T \tag{EQ17}$$

The loci on the body reflection plane and the specular reflection plane is shown in Figure 6. Note that the dimension of the temporal-color space is reduced from four to three for clarity. In this diagram, the blue channel is omitted.

Section 4 Experimental Results

4.1. Experimental setup

The algorithm outlined in this report was applied to color images of several kinds of objects, a shiny dielectric object, a matte dielectric object, and a metal object, in order to demonstrate the feasibility of the proposed algorithm. The surface normal and the albedo of the objects were obtained using the algorithm. The algorithm was applied to the metal object to demonstrate that it also works in the case where only the specular reflection component exits. The algorithm was subsequently applied to each pixel of the entire image to extract the needle map of the object in the image. The object shape was recovered from the needle map. Finally, the decomposed two reflection components are used to create image sequences of each of the two reflection components.

In our experiment, a lamp shade whose diameter is 20 inches is used as the light diffuser. The object is placed inside the spherical diffuser. It is important to note that the use of the light diffuser for generating an extended light source is not essential for the algorithm to separate two reflection components. It is only used for avoiding camera saturation when input images are taken. With the light diffuser, highlights observed on objects become less bright and distributed in larger area of the objects' surfaces. The algorithm introduced in the paper can be applied to images taken without a light diffuser when the objects are not very shiny.

A SONY CCD video camera module model XC-57 to which three color filters (#25, #58, #47) are attached, is placed at the top of the diffuser. A point light source attached to a PUMA 560 manipulator is moved around the diffuser on its equatorial plane. The whole system is controlled by a SUN SPARC workstation through a LISP program. A geometry of the experimental setup is shown in Figure 10. The maximum dispersion angle α (EQ31) of the extended light source is determined by the fixed diameter R and the distance from the point light source to the surface of the diffuser H which is controlled from a workstation (Figure 31).

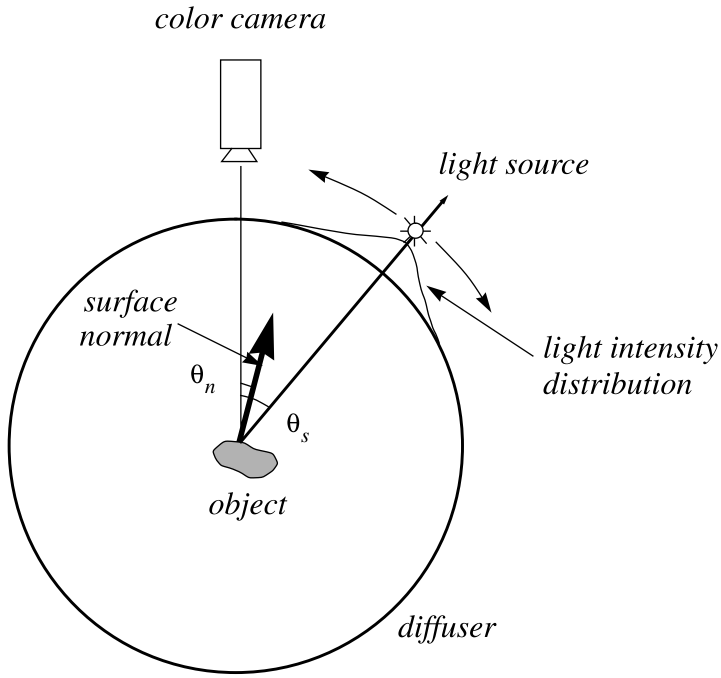

Figure 10 The geometry of the experimental setup

4.2. Fitting algorithm

After the geometry matrix D has been recovered, the two curves ((EQ18) and (EQ19)) are fitted to the body and specular reflection components, respectively. A gaussian curve is used as the approximation of $L(2\theta_n - \theta_s)$ ((EQ30), (EQ31), and (EQ33)) of the specular reflection component.

$$A_1 \cos(\theta_s - A_2) + A_3 \tag{EQ18}$$

$$B_1 exp\left(\frac{-(\theta_s - B_2)^2}{B_3^2}\right) \tag{EQ19}$$

$B_2/2$ and A_2 are the direction of the surface normal. B_1 and A_1 are the albedos of the specular and body reflection components, respectively.

4.3. A shiny dielectric object

A green plastic cylinder with relatively smooth surface was used in this experiment (Figure 11).

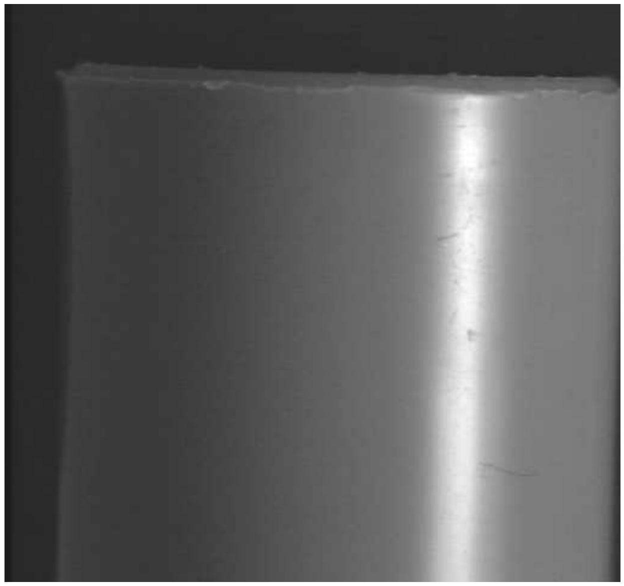

Figure 11 Green shiny plastic cylinder

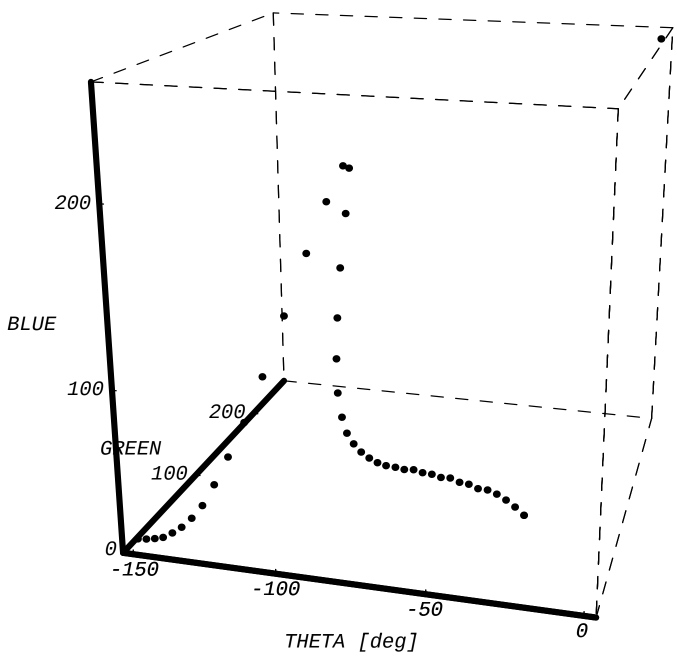

Figure 12 Measured intensities in the temporal-color space

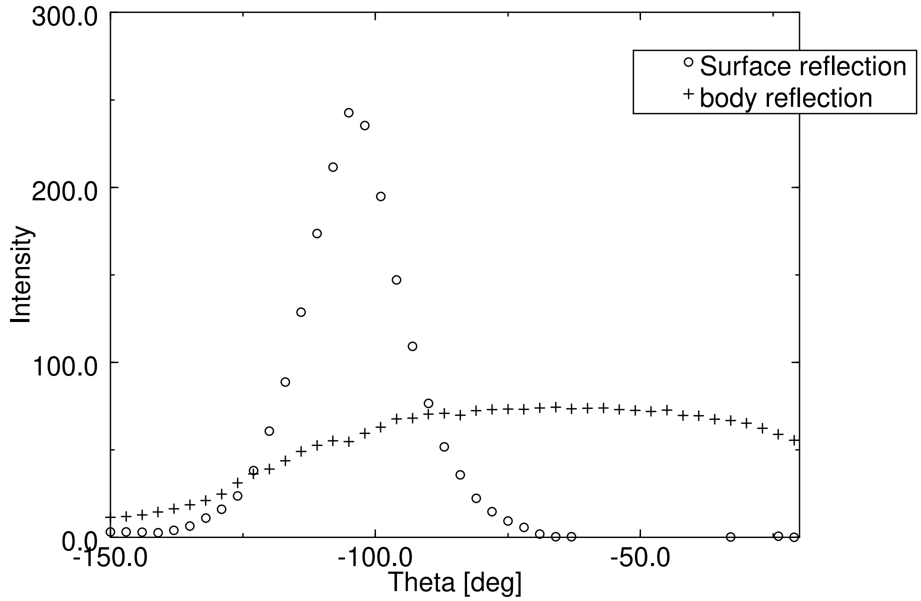

Figure 13 Decomposed two reflection components

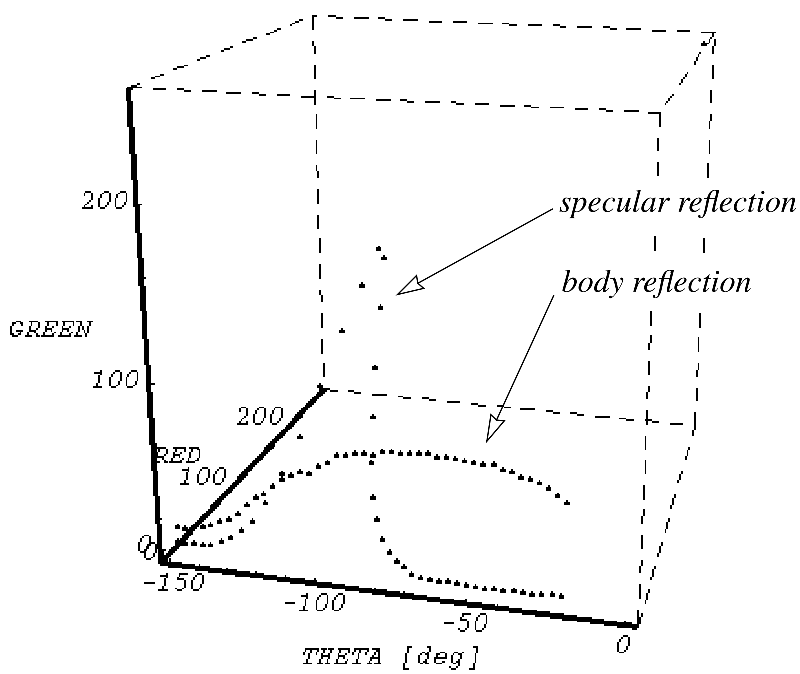

Figure 14 Loci of two reflection components in the temporal-color space

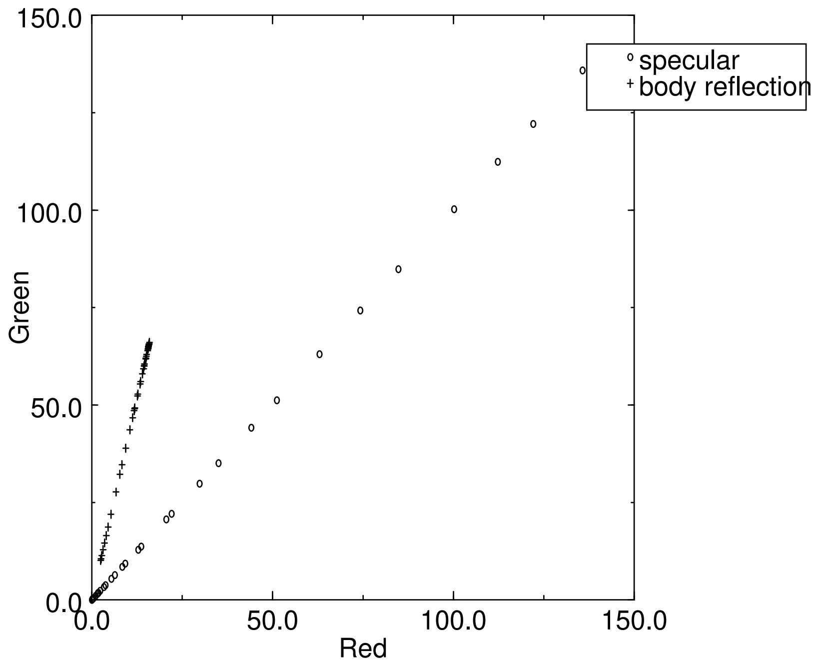

Figure 15 The body reflection plane and the specular reflection plane

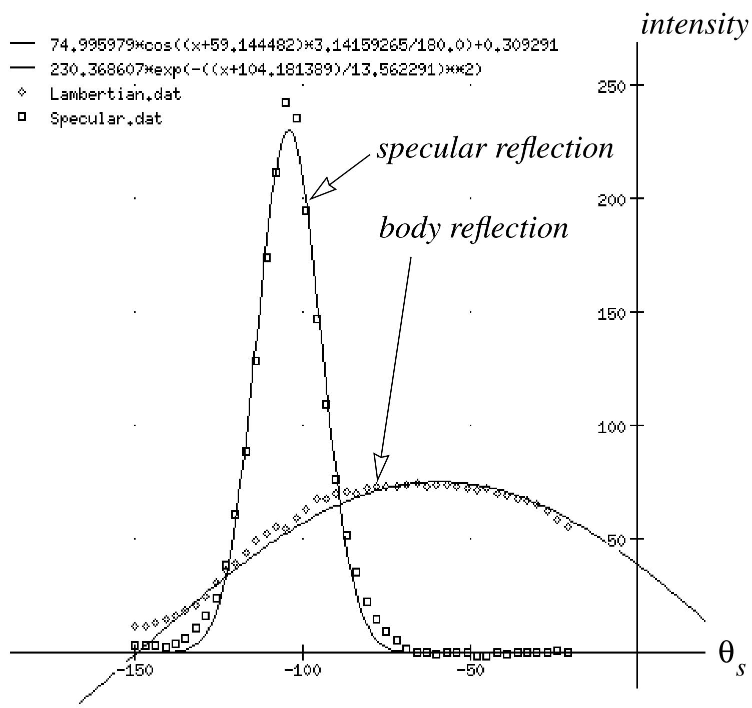

Figure 16 The result of fitting

Figure 12 shows the measured intensities plotted in the temporal-color space with the blue axis omitted. The intensity values were normalized by using the sensor model explained in [19].

Note that the intensity values around the maximum intensity contain both the body reflection component and the specular reflection component (EQ9). On the other hand, the intensity values for $\theta_s > -60°$ contain only the body reflection component. The curve for $\theta_s > -60°$ and $\theta_s < -140°$ lies inside the body reflection plane in the temporal-color space, whereas the curve for $-140° < \theta_s < -60°$ does not lie inside the body reflection plane. This is because the intensities values for $-140° < \theta_s < -60°$ are linear combinations of the body color vector $\underset{\sim}{K}_L$ and the specular color vector $\underset{\sim}{K}_S$.

The algorithm for separating the two reflection components, described in Section 3.2, was applied to the measured data. The red, green, and blue intensities are initially stored into the temporal-color matrix I as its columns (Figure 5 and (EQ12)). Then, the temporal-color matrix I is decomposed into the geometry matrix D and the color matrix K. The columns of the resulting geometric matrix D is plotted in Figure 13. Note that the body reflection component and the specular reflection component have the shapes corresponding to the functions $\cos(\theta_s - \theta_n)$ and $L(\theta_s - 2\theta_n)$, respectively, as shown in (EQ9). Figure 14 shows the result of the decomposition of the reflection in the temporal-color space. It is evident from this figure that the measured intensity in the temporal-color space (Figure 12) has been successfully decomposed into the body and specular reflection components using our algorithm described in Section 3.2.

The body reflection plane and the specular reflection plane are shown in Figure 15. This diagram is the result of viewing Figure 14 along the θ_s axis. Note that the slope of the specular reflection plane is $45°$ in the diagram. This is because the specular reflection vector (EQ11) has been normalized to

$$\underset{\sim}{K}_S = \left(\frac{1}{\sqrt{3}}, \frac{1}{\sqrt{3}}, \frac{1}{\sqrt{3}}\right) \qquad \textbf{(EQ20)}$$

The body reflection plane is shifted towards the green axis because the color of the observed object is green in this experiment.

The result of the fitting procedure described in Section 4.2 is shown in Figure 16. From the result, we obtain the direction of the surface normal, and the albedos as the follows: the surface normal $(B_2/2)$ $-52.09°$, the albedo of the specular reflection component (B_1) 230.37, and the albedo of the body reflection component (A_1) 75.00. Notations A_1, B_1, and B_2 follow (EQ18) and (EQ19).

4.4. A matte dielectric object

A green plastic cylinder with a relatively rough surface was used in this experiment (Figure 17).

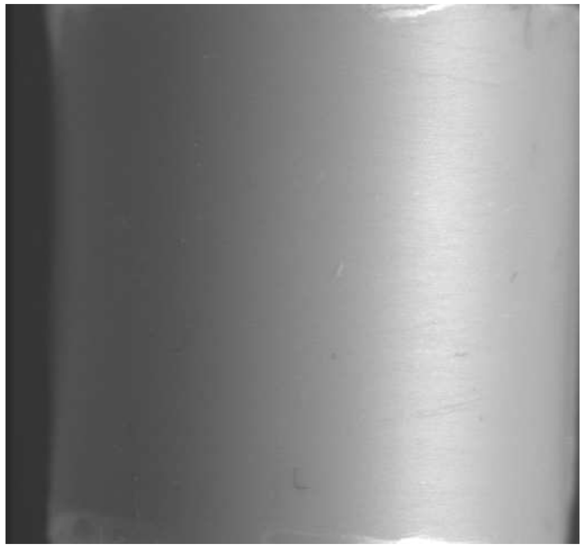

Figure 17 Green matte plastic cylinder

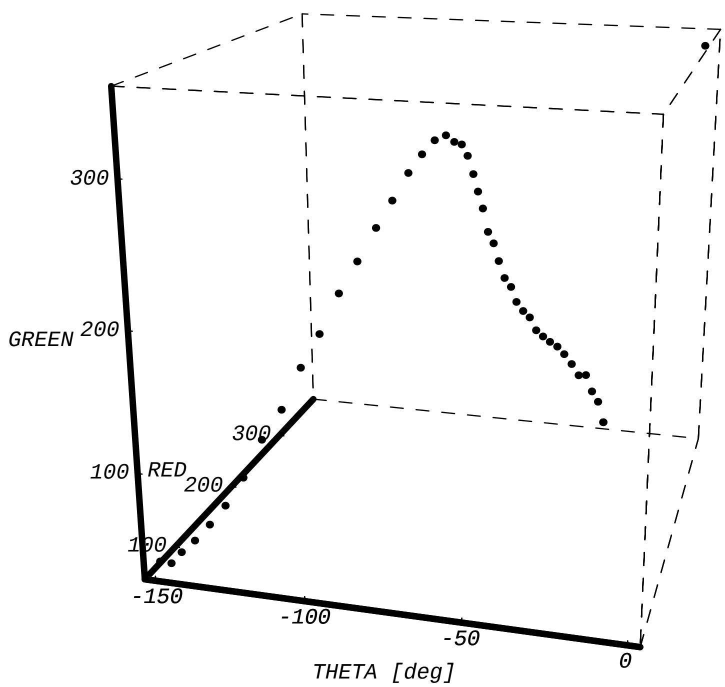

Figure 18 Measured intensities in the temporal-color space

The measured intensities are plotted in the temporal-color space (Figure 18) in the same manner as explained in Section 3.2. Note that the width of the specular reflection component is larger than that in the previous experiment. This is mainly attributed to different surface roughness of two plastic cylinders. It seems that the width can be an important and revealing indication of surface roughness from observed images. The interpretation of the width is a subject of further study.

The intensity is decomposed into the two reflection components according to the algorithm shown in Section 3.2. The result of the decomposition is shown in Figure 19. Note that the directions of the specular reflection plane and the body reflection plane are same as those in the case of the previous shiny green plastic cylinder. The specular reflection plane does not change its direction because the color of the specular reflection component $\underset{\sim}{K}_S$ is that of the light source (Figure 6). In other words, the specular reflection component has the same spectral as the light source. Also, the correspondence of the direction of the body reflection component is due to similarity of surface colors of the two plastic objects despite of their different surface roughness.

Figure 20 depicts the result of curve fitting to the decomposed two reflection components. The surface normal and the albedos of the two reflection components obtained are: the surface normal ($B_2/2$) $-49.61°$, the albedo of the specular reflection component (B_1) 219.83, and the albedo of the body reflection component (A_1) 308.1.

Note that the standard deviation of the Gaussian curve representing the specular reflection component (B_3 in (EQ19)) is 26.68. This value is greater than that of the shiny plastic object (13.56). The difference is consistent with the fact that the matte object's surface roughness is larger than the shiny object's surface roughness. Further study is necessary to make any quantitative statement about the relationship between the standard deviation and the surface roughness.

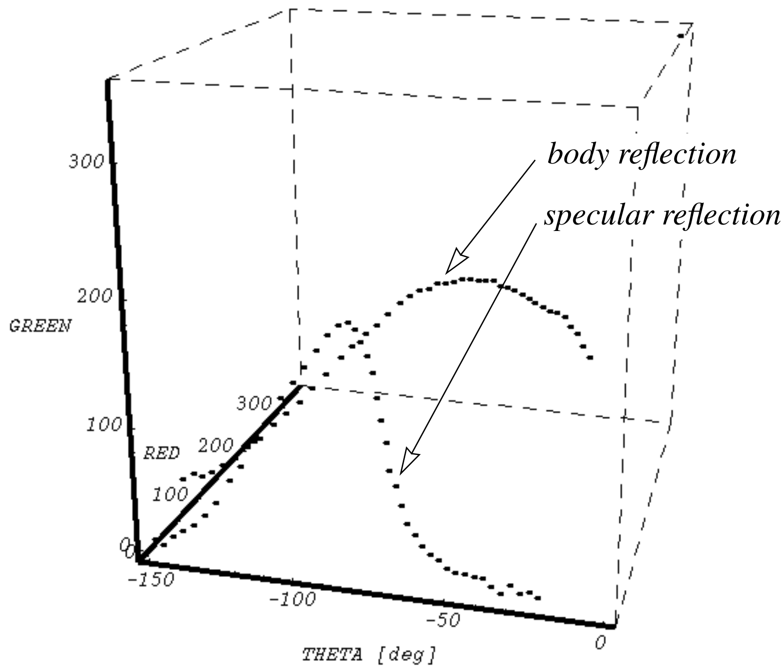

Figure 19 Decomposed two reflection components

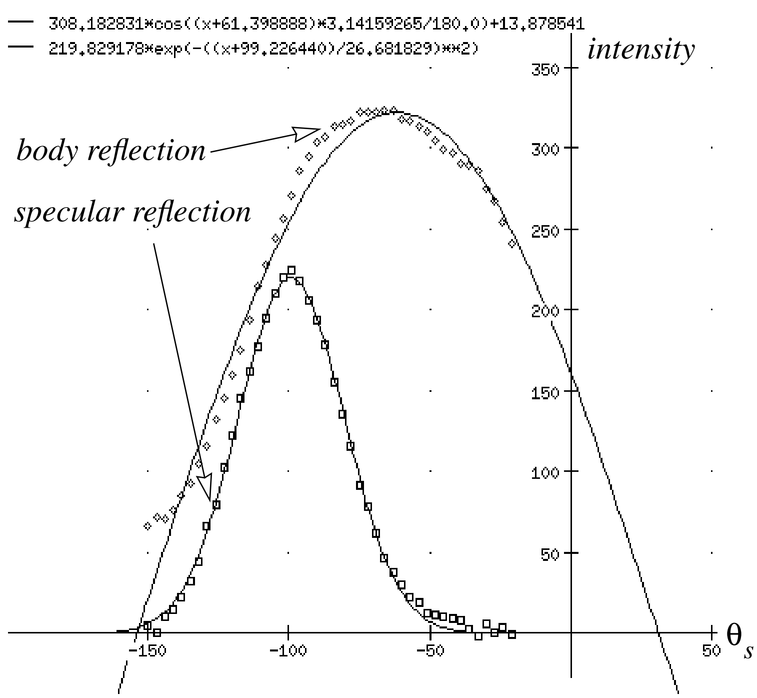

Figure 20 The result of fitting

4.5. A metal object

The dichromatic reflection model [22] cannot be applied to non-dielectric objects such as a metallic specular object. As an example of those objects, an aluminum triangular prism was used in this experiment (Figure 21). This type of material does not have the body reflection component but only the specular reflection component. This results in the fact that the matrix I has a rank of 1 when the object is metallic.

The measured intensities shown in Figure 22 indicate that the reflection from the aluminum triangular prism possesses only the specular reflection component. This observation is justified by the result of the decomposition of the two reflection components (Figure 23). The body reflection component is negligibly small compared to the specular reflection component.

Figure 21 Aluminum triangular prism

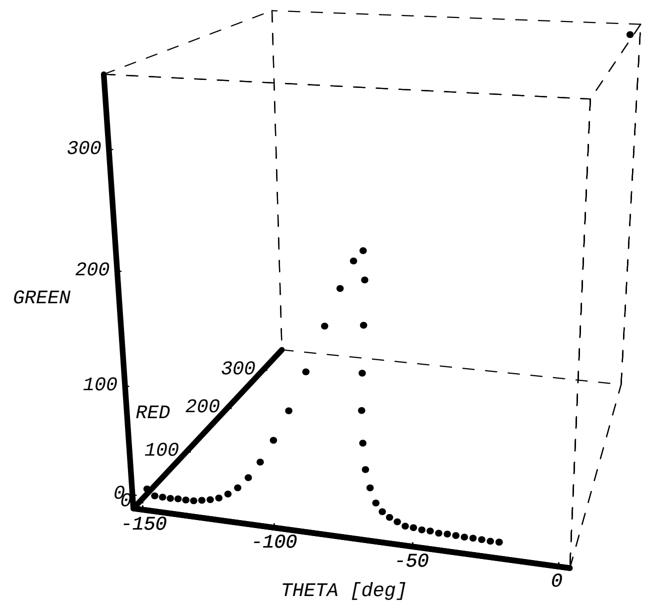

Figure 22 Locus of the intensity in the temporal-color space

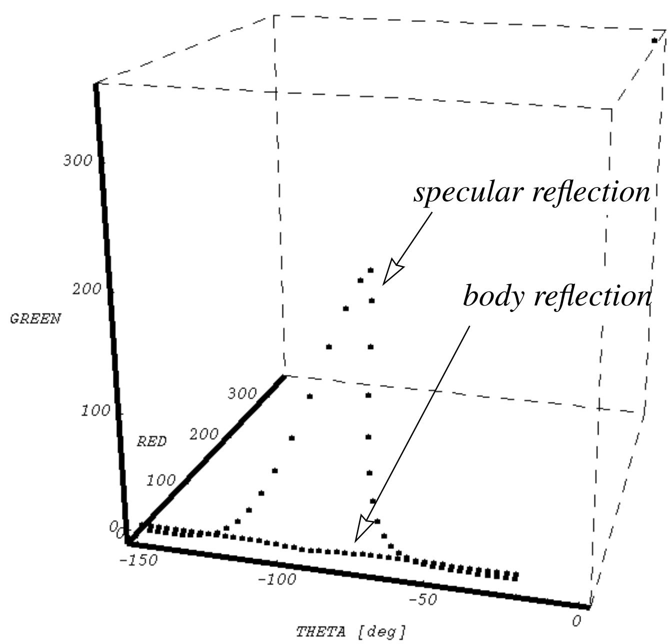

Figure 23 Decomposed two reflection components

4.6. Shape recovery

In the previous sections, the decomposition algorithm was applied to real color images in order to separate the two reflection components using intensity change at a *single* pixel. In other words, the reflection components were separated *locally.* After this separation, the surface normal and albedo at each pixel were obtained by nonlinear curve fitting of the two reflection components models ((EQ18) and (EQ19)) to the decomposed reflection components. The surface normal of the pixel is $B_2/2$ and A_2, and the albedos are B_1 and A_1 in those equations. We repeated the same operation over all pixels in the image to obtain surface normals over the entire image. Then, the needle map and the depth map of the object in the image were obtained from those recovered surface normals.

We used a purple plastic cylinder as the observed object in this experiment. The image is shown in Figure 24. Results of the curve fitting of the body reflection component were used to obtain surface normal directions. The resulting needle map is shown in Figure 25. The depth map of the purple plastic cylinder is obtained by a simple integration method. Figure 26 depicts the resulting depth map.

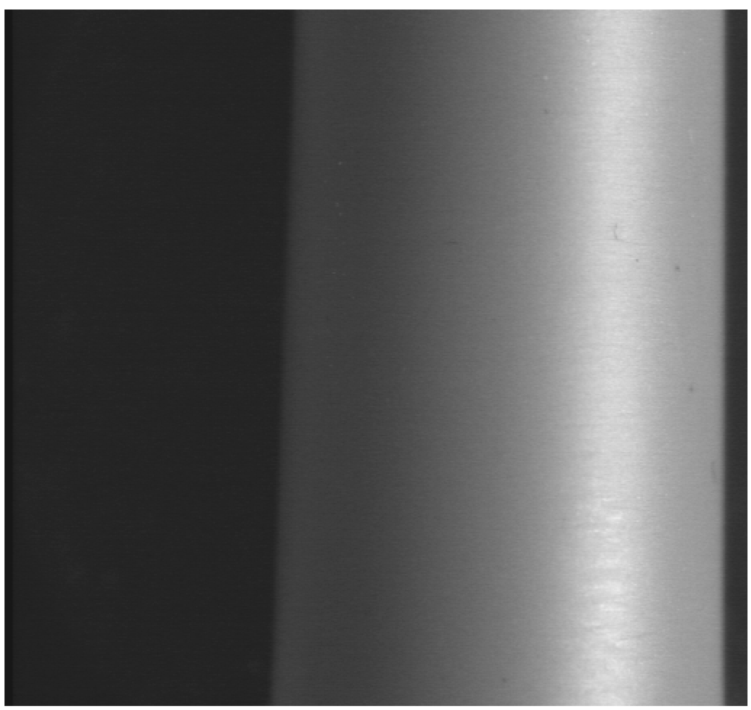

Figure 24 Purple plastic cylinder

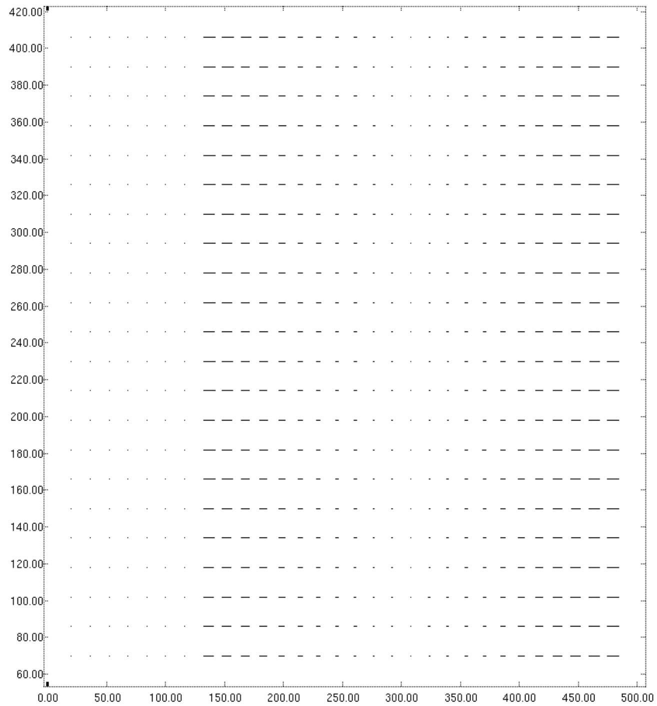

Figure 25 Needle map

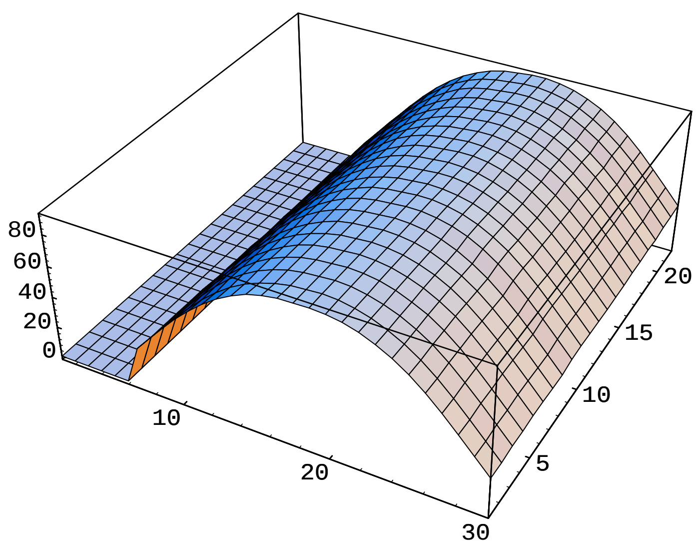

Figure 26 Recovered object shape

4.7. Generating body reflection image and specular reflection image

By using the pixel-based separation algorithm, we can easily generate images of the two reflection components. The algorithm was applied to all pixels of the input images locally, and each separated reflection component was used to generate the body reflection image and the specular reflection image. Figure 27 shows one frame from the input image sequence. All pixels in the image are decomposed into two reflection components by using the algorithm described in this paper. The result of the body reflection image and the specular reflection image are shown in Figure 28 and Figure 29, respectively. Note that the input image is successfully decomposed into the images of the two reflection components, even though the input image has a complex object with many color regions on the surface. This is because the proposed algorithm is pixel-based and does not require global information. In this kind of situation, the traditional separation algorithm based on the RGB color histogram would easily fail because clusters in the RGB color space become crowded and obscure, so that clustering in the RGB space becomes impossible. On the other hand, since our algorithm is pixel-based and applied to each pixel separately, the two reflection components can be successfully separated even in the face of inconspicuous specular reflection.

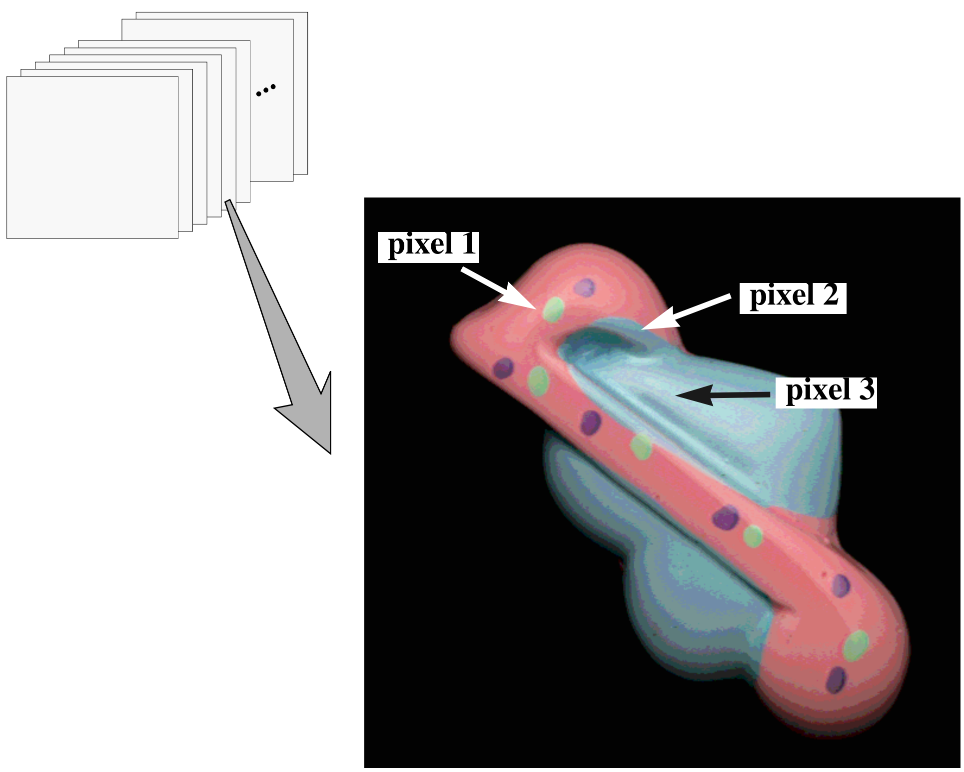

Figure 27 Multicolored object

The three pixels of different colors are manually selected in the image.

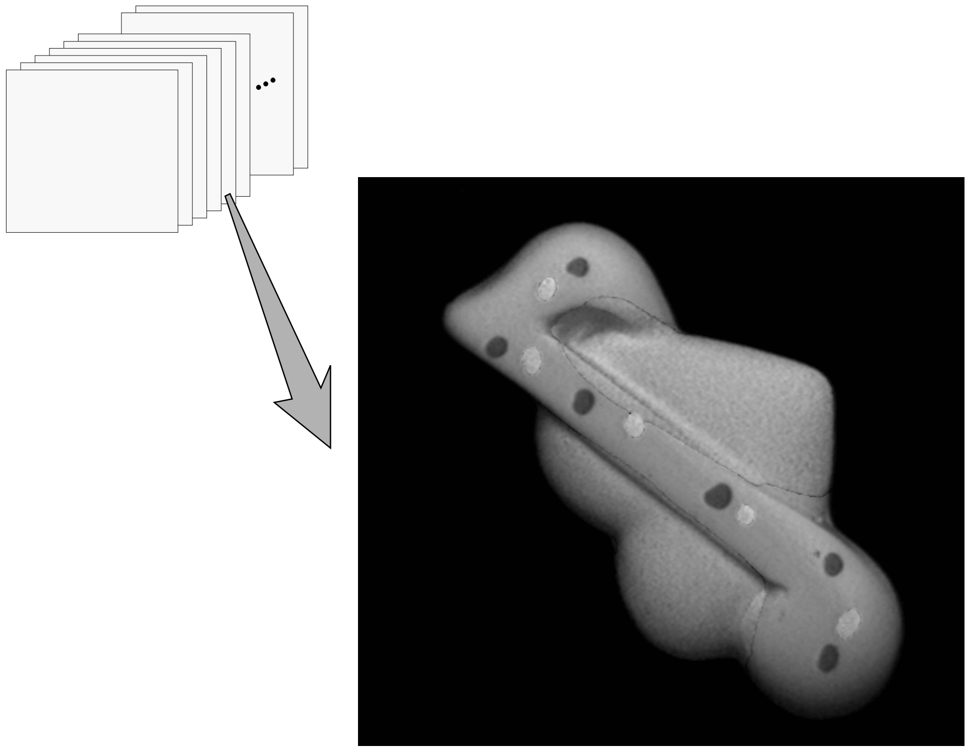

Figure 28 Body reflection image

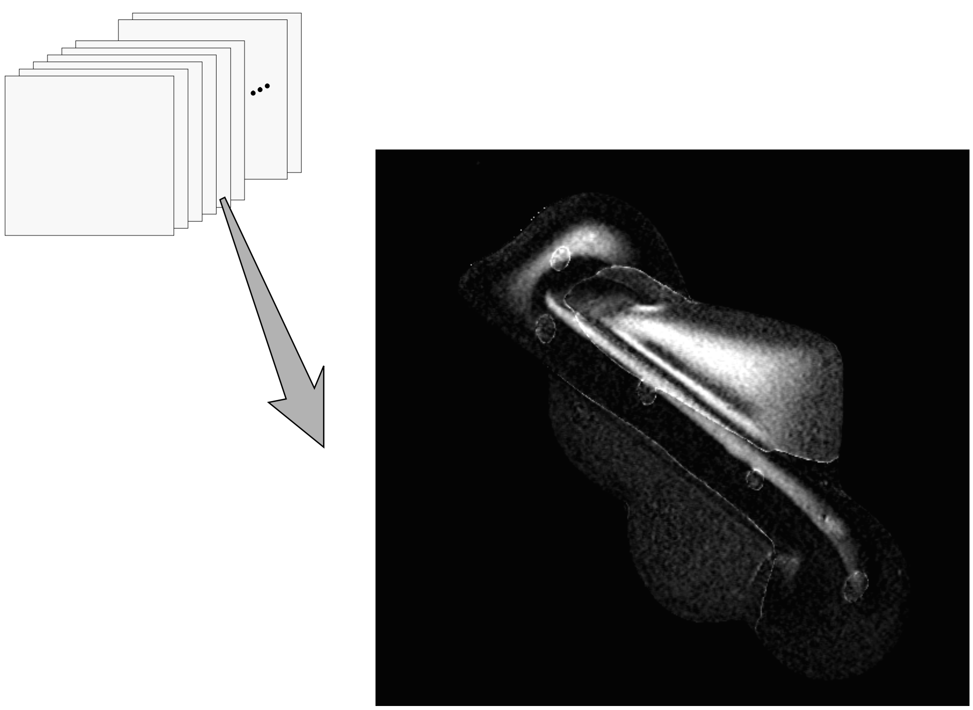

Figure 29 Specular reflection image

Section 5 Conclusions

We propose temporal-color space analysis as a new concept for color image analysis, where the body reflection component and the specular reflection component from the dichromatic reflection model span subspaces. We have presented an algorithm to separate the two reflection components at each pixel from a sequence of color images and to obtain the surface normal and the albedo without prior knowledge of the reflectance properties. The significance of our method lies in its use of local (i.e., pixel-based) and not global information of intensity values in the images. This characteristic separates our algorithm from previously proposed algorithms for segmenting the body reflection component and the specular reflection component in the RGB color space.

Our algorithm has been applied to objects of different materials to demonstrate the algorithm's effectiveness. We have successfully separated the two reflection components in the temporal-color space and have obtained surface normals and albedos of the two reflection components. In addition, we are able to reconstruct the shape of the objects.

Acknowledgments

The authors are thankful to the anonymous reviewers and Fredric Solomon for their constructive criticism, which resulted in a significant improvement in the quality of this paper. We would also like to thank Sing Bing Kang, Kevin Lynch, and Kathryn Porsche for their valuable suggestions on the manuscript.

Appendix A: Hybrid reflectance model

A mechanism of reflection is described in terms of three reflection components, namely the specular spike, the specular lobe, and the diffuse lobe. These reflection components are represented by the Beckmann-Spizzichino model, the Torrance-Sparrow model (or the Beckmann-Spizzichino model), and the Lambertian model, respectively. The model of reflection mechanism which accounts for all three components is usually too complicated to be used for actual applications: it is useful to simplify this reflection model into a simpler model [14]. On a very rough surface, distributions of the specular spike and the specular lobe with respect to a light source direction θ_i have a large overlap around a specular angle. As a result, it is not easy to separate these two components. On the other hand, the two distributions converge into a narrow angle around the specular angle when a wavelength is comparable to the surface roughness, i.e., when the surface is reasonably smooth. Therefore, the specular spike and the specular lobe can be combined as the *specular reflection component* as a reasonable approximation [14]. A unit impulse function is used to approximate the specular component. The Lambertian model is also used to represent the diffuser lobe component which is also called the *body reflection component.* The reflectance model which has the specular and body reflection components is named the hybrid reflectance model by Nayar [14]. Nayar used the hybrid reflectance model for analyzing reflection, which includes both the surface and body reflection components [14]. In the hybrid reflectance model, the intensity of an image in each pixel is expressed as

$$I = I_L + I_S \tag{EQ21}$$

where I_L is the body reflection component and I_S is the specular reflection component.

The dichromatic reflection model in the two dimensional planar case can be represented in terms of the bidirectional spectral-reflectance distribution function (BSRDF) proposed by Nicodemus *et al.* [17] as:

$$f_r(\theta_i, \theta_r, \lambda) = c_L(\lambda)\, g_L(\theta_i, \theta_r) + c_S(\lambda)\, g_S(\theta_i, \theta_r) \tag{EQ22}$$

where f_r is the BSRDF, $c_L(\lambda)$ and $c_S(\lambda)$ are the spectral reflectance distributions, and $g_L(\theta_i, \theta_r)$ and $g_S(\theta_i, \theta_r)$ are the geometrical terms. The subscripts L and S refer to the body reflection component and the specular reflection component, respectively. θ_i and θ_r are the incident angle and the reflecting angle, respectively, as shown in Figure 30.

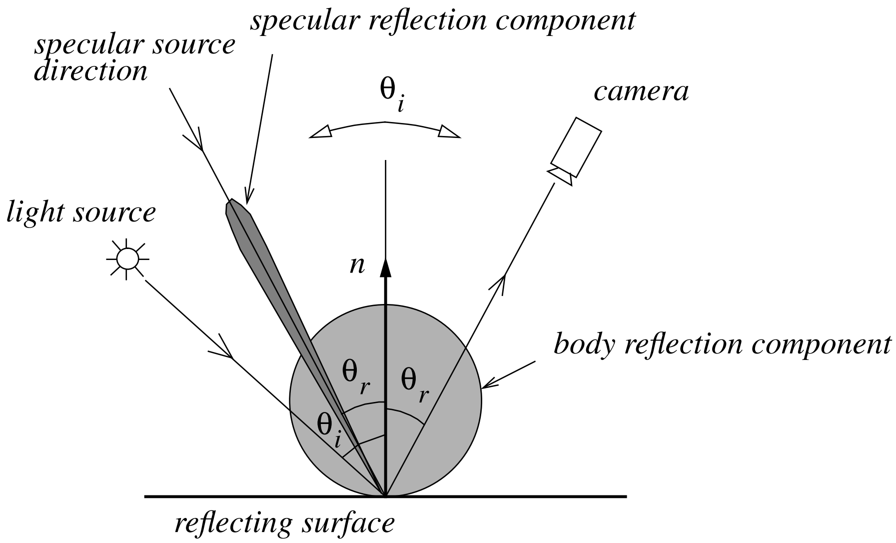

Figure 30 Hybrid reflectance model

In most reflection models, it is assumed that the body reflection component has a spectral distribution different from that of an incident light, while the surface reflection component has the similar spectral distribution. Lee called this model the neutral-interface-reflection (NIR) model [12]. Considering the NIR model, (EQ22) is written as:

$$f_r(\theta_i, \theta_r, \lambda) = c_L(\lambda)\, g_L(\theta_i, \theta_r) + c_S g_S(\theta_i, \theta_r) \qquad \textbf{(EQ23)}$$

Since we assumed that the body reflection component is modeled by the Lambertian model, and the surface reflection component is modeled by a unit impulse function, geometrical terms $g_L(\theta_i, \theta_r)$ and $g_S(\theta_i, \theta_r)$ in (EQ23) become

$$g_L(\theta_i, \theta_r) = max[0, \cos\theta_i]$$

$$g_S(\theta_i, \theta_r) = \delta(\theta_i - \theta_r) \qquad \textbf{(EQ24)}$$

Substituting (EQ24) into (EQ23), we get

$$f_r(\theta_i, \theta_r, \lambda) = c_L(\lambda)\cos\theta_i + c_S\delta(\theta_i - \theta_r) \qquad \textbf{(EQ25)}$$

On the other hand, the intensity of incident light onto the object surface (and not into the camera) is represented as:

$$L_i(\theta_i, \lambda) = c(\lambda)\, L(\theta_i) \qquad \textbf{(EQ26)}$$

where $c(\lambda)$ is the spectral distribution and $L(\theta_i)$ is a geometrical term of incident light onto the object surface. The intensity of light reflected on the object surface and coming into the camera can be expressed as the product of $L_i(\theta_i, \lambda)$ and the BSRDF $f_r(\theta_i, \theta_r, \lambda)$. Finally, the pixel value I is given by:

$$\begin{aligned} I(\theta_i, \theta_r) &= \int_{\lambda} s(\lambda) L_i(\theta_i, \lambda) f_r(\theta_i, \theta_r, \lambda)\, d\lambda \\ &= \int_{\lambda} s(\lambda) c(\lambda) L(\theta_i) \{c_L \cos\theta_i + c_S \delta(\theta_i - \theta_r)\}\, d\lambda \\ &= L(\theta_i) \cos\theta_i \int_{\lambda} s(\lambda) c(\lambda) c_L(\lambda)\, d\lambda + \\ &\quad L(\theta_i)\, \delta(\theta_i - \theta_r)\, c_S \int_{\lambda} s(\lambda) c(\lambda)\, d\lambda \end{aligned} \tag{EQ27}$$

where $s(\lambda)$ is the spectral response of a camera.

The hybrid reflectance model is expressed by (EQ27). Changing the coordinate system into the viewer-centered coordinate system shown in Figure 2, (EQ27) becomes

$$I(\theta_s) = K_L L(\theta_s - \theta_n) \cos(\theta_s - \theta_n) + K_S L(\theta_s - \theta_n)\, \delta(2\theta_n - \theta_s) \tag{EQ28}$$

where

$$\begin{aligned} K_L &= \int_{\lambda} s(\lambda) c(\lambda) c_L(\lambda)\, d\lambda \\ K_S &= c_s \int_{\lambda} s(\lambda) c(\lambda)\, d\lambda \end{aligned} \tag{EQ29}$$

Appendix B: Extended light source

An extended light source is used in our experiments instead of a point light source. The extended light source is generated by a spherical diffuser which is composed of white light-diffusing material. The geometry of the diffuser is shown in Figure 31.

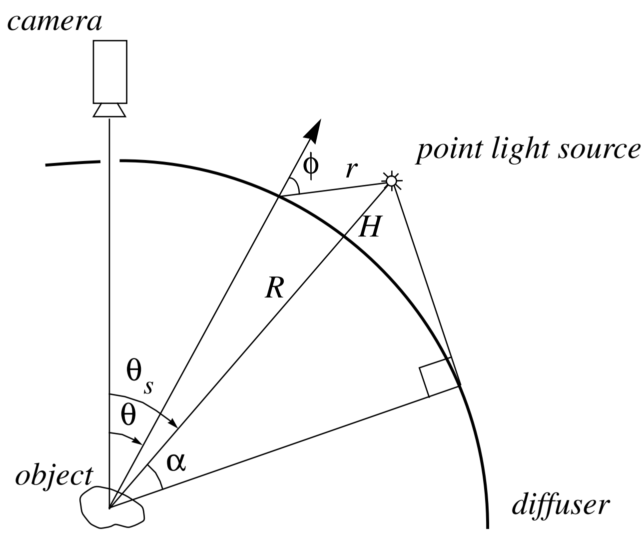

Figure 31 Geometry of the extended light source

The distribution of the extended light source is given by:

$$L(\theta_i) = L(\theta - \theta_s) = \frac{CJ[(R+H)\cos(\theta-\theta_s) - R]}{\left[(R+H-R\cos(\theta-\theta_s))^2 + (R\sin(\theta-\theta_s))^2\right]^{3/2}} \quad \textbf{(EQ30)}$$

This distribution is limited to the interval $\theta_s - \alpha < \theta < \theta_s + \alpha$ where

$$\alpha = \operatorname{acos}\frac{R}{R+H} \quad \textbf{(EQ31)}$$

A derivation of this formula is shown in Appendix of [14].

The hybrid reflectance model (EQ7) can be rewritten using the extended light source as follows:

$$I(\theta_s) = \int_{(\theta_s - \alpha)}^{(\theta_s + \alpha)} L(\theta, \theta_s) \cos(\theta - \theta_n) \int_{\lambda} \tau(\lambda) s(\lambda) c(\lambda) c_L(\lambda) d\lambda d\theta +$$

$$\int_{(\theta_s - \alpha)}^{(\theta_s + \alpha)} L(\theta, \theta_s) \delta(\theta - 2\theta_n) c_S \int_{\lambda} \tau(\lambda) s(\lambda) c(\lambda) d\lambda d\theta$$

$$= \int_{\lambda} \tau(\lambda) s(\lambda) c(\lambda) c_L(\lambda) d\lambda \cos(\theta_s - \theta_n) +$$

$$c_S \int_{\lambda} \tau(\lambda) s(\lambda) c(\lambda) d\lambda L(\theta_s, 2\theta_n)$$

(EQ32)

Therefore,

$$I(\theta_s) = K_L \cos(\theta_s - \theta_n) + K_S L(\theta_s - 2\theta_n)$$ **(EQ33)**

where

$$K_L = \int_{\lambda} \tau(\lambda) s(\lambda) c(\lambda) c_L(\lambda) d\lambda$$

$$K_S = c_S \int_{\lambda} \tau(\lambda) s(\lambda) c(\lambda) d\lambda$$

(EQ34)

(EQ33) shows that the intensity curve with respect to a direction of the extended light source is a linear combination of a cosine curve representing the body reflection component and the $L(\theta_s - 2\theta_n)$ curve representing the specular reflection component (Figure 32).

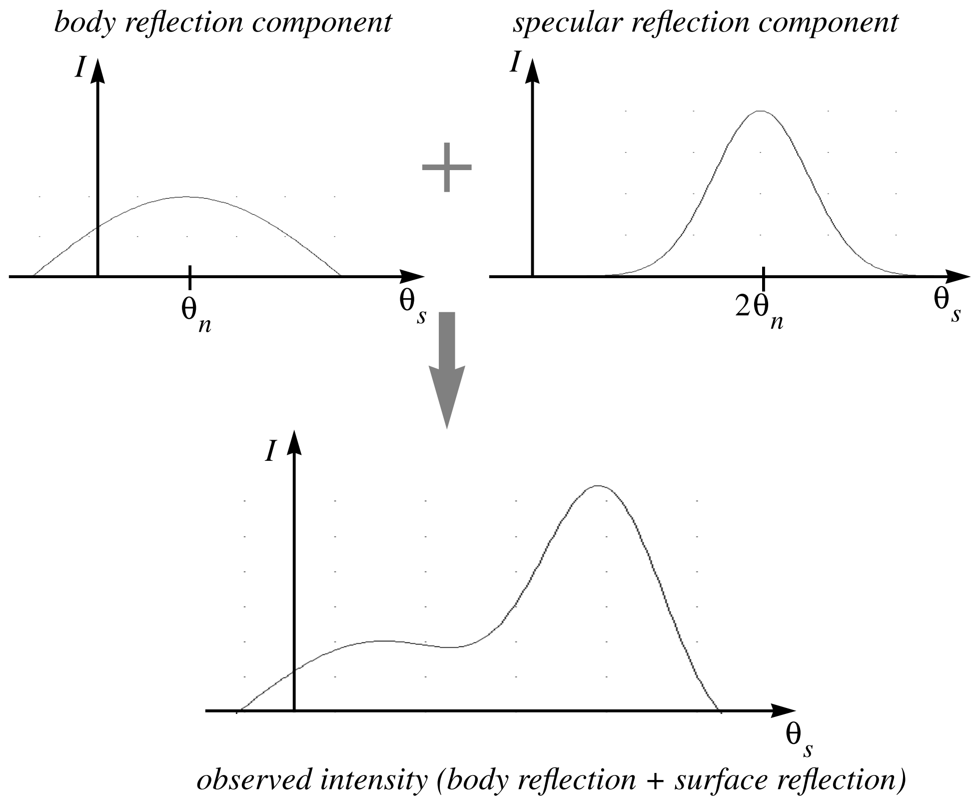

Figure 32 Two reflection components under an extended light source

References

[1] R. Bajcsy, S. W. Lee, A. Leonardis, "Color image segmentation with detection of highlights and local illumination induced by inter-reflections," *Proc. 10th Int. Conf. on Pattern Recognition,* Vol I, pp. 785-790, 1990.

[2] B. V. Funt and M. S. Drew, "Color space analysis of mutual illumination," *IEEE Transactions on Pattern Analysis and Machine Intelligence*, Vol. 15, No. 12, pp. 1319-1326, December 1993.

[3] R. M. Haralick and G. L. Kelly, "Pattern recognition with measurement space and spatial clustering for multiple images," *Proc. IEEE*, 57:pp. 654-665, April 1969.

[4] G. Healey, "Using color for geometry-insensitive segmentation," *Journal of Optical Society of America A*, Vol. 6, No. 6, pp. 920-937, June 1989.

[5] G. Healey and T. Binford, "Local shape from specularity," *Computer Vision, Graphics and Image Processing*, Vol. 42, No. 1, pp. 62-86, April 1988.

[6] J. Ho, B. V. Funt, M. S. Drew, "Separating a color signal into illumination and surface reflectance components: Theory and applications," *IEEE Transactions on Pattern Analysis and Machine Intelligence*, Vol. 12, No. 10, pp. 966-977, 1990.

[7] B. K. P. Horn, "Obtaining shape from shading information," in B. K. P. Horn and M. J. Brooks (Ed.), *Shape from Shading*, MIT Press, pp. 123-171, Cambridge, 1989.

[8] K. Ikeuchi and B. K. P. Horn, "Numerical shape from shading and occluding boundaries," *Artificial Intelligence,* Vol. 17, pp. 141-184, August 1981.

[9] K. Ikeuchi, "Determining surface orientations of specular surfaces by using the photometric stereo method," *IEEE Transactions on Pattern Analysis and Machine Intelligence*, Vol. 3, No. 6, pp. 661-669, 1991.

[10] G. J. Klinker, S. A. Shafer, and T. Kanade, "The measurement of highlight in color images," *International Journal of Computer Vision (IJCV)*, Vol. 2, No. 1, pp. 7-32, 1988.

[11] G. J. Klinker, S. A. Shafer, and T. Kanade, "A physical approach to color image understanding," *International Journal of Computer Vision (IJCV)*, Vol. 4, No. 1, pp. 7-38, 1990.

[12] H. C. Lee, E. J. Breneman, and C. P. Schulte, "Modeling light reflection for computer color vision," *IEEE Transactions on Pattern Analysis and Machine Intelligence*, Vol. 12, No. 4, pp. 402-409, April 1990.

[13] H. C. Lee, "Method for computing the scene-illuminant chromaticity from specular highlights," *J. Opt. Soc. Am. A,* Vol. 3, No. 10, pp. 1694-1699, 1986.

[14] S. K. Nayar, K. Ikeuchi, and T. Kanade, "Determining shape and reflectance of hybrid surfaces by photometric sampling," *IEEE Trans. on Robotics and Automation*, Vol. 6, No. 4, pp. 418-431, 1990.

[15] S. K. Nayar, K. Ikeuchi, and T. Kanade, "Surface reflection: Physical and geometrical perspectives," *IEEE Transaction on Pattern Analysis and Machine Intelligence,* Vol. 13, No. 7, pp. 611-634, July 1991.

[16] S. K. Nayar, X. Fang, and T. Boult, "Removal of specularities using color and polarization," *Proceedings of IEEE Conference on Computer Vision and Pattern Recognition*, pp. 583-589, 1993.

[17] F. E. Nicodemus, J. C. Richmond, J.J. Hsia, I. W. Ginsberg, and T. Limperis, "Geometrical considerations and nonmenclature for reflectance," U. S. Bureau Standards (U. S.), Monograph 160, Oct. 1977.

[18] C. L. Novak, "Anatomy of a histogram," *Proceedings of IEEE Conference on Computer Vision and Pattern Recognition*, pp. 599-605, 1992.

[19] C. L. Novak, S. A. Shafer, and R. G. Willson, "Obtaining accurate color images for machine vision research," *SPIE Proceedings*, Vol. 1250, pp. 54-68, Feb. 1990.

[20] H. Sato, S. K. Nayar, and K. Ikeuchi, "Implementation and evaluation of a three-dimensional photometric sampler," Technical Report CMU-CS-92-148, Department of Computer Science, Carnegie Mellon University, 1992.

[21] S. A. Shafer, "Optical phenomena in computer vision," In *Proceedings CSCSI-84*, Lon-

don, Ontario, May 1984. Canadian Society for Computational Studies of Intelligence.

[22] S. A. Shafer, "Using color to separate reflection components," *COLOR Research and Application*, Vol. 10, No. 4, pp. 210-218, 1985.

[23] S. Tominaga and B. A. Wandell, "Standard surface-reflectance model and illuminant estimation," *Journal of Optical Society of America A*, Vol. 6, No. 4, pp. 576-584, April 1989.

[24] K. Torrance and E. Sparrow, "Theory for off-specular reflection from roughened surfaces," *Journal of the Optical Society of America,* No. 57, pp. 1105 - 1114, 1967.

[25] R. J. Woodham, "Photometric Stereo: A reflectance map technique for determining surface orientation from image intensity," Proc. SPIE, Vol. 155, pp. 136-143, 1978.

[26] L.B. Wolff, "Using polarization to separate reflection components," *Proceedings of IEEE Conference on Computer Vision and Pattern Recognition*, pp. 363-369, 1989.